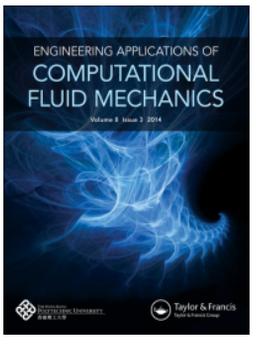

Taylor & Francis
Taylor & Francis Group

Engineering Applications of Computational Fluid Mechanics

ISSN: (Print) (Online) Journal homepage: www.tandfonline.com/journals/tcfm20

Aerodynamic impact of wind-sand flow on moving trains in tunnel-embankment transition section: from field testing to CFD modeling

E Deng, Huan Yue, Xin-Yuan Liu & Yi-Qing Ni

To cite this article: E Deng, Huan Yue, Xin-Yuan Liu & Yi-Qing Ni (2023) Aerodynamic impact of wind-sand flow on moving trains in tunnel-embankment transition section: from field testing to CFD modeling, Engineering Applications of Computational Fluid Mechanics, 17:1, 2279993, DOI: 10.1080/19942060.2023.2279993

To link to this article: https://doi.org/10.1080/19942060.2023.2279993

Published online: 14 Nov 2023.

ENGINEERING APPLICATIONS OF COMPUTATIONAL FLUID MECHANICS
2023, VOL. 17, NO. 1, 2279993
https://doi.org/10.1080/19942060.2023.2279993

Aerodynamic impact of wind-sand flow on moving trains in tunnel-embankment transition section: from field testing to CFD modeling

E Deng[a,b], Huan Yue[a,b], Xin-Yuan Liu[a,b] and Yi-Qing Ni[a,b]

[a]National Rail Transit Electrification and Automation Engineering Technology Research Center (Hong Kong Branch), Hong Kong, People's Republic of China; [b]Department of Civil and Environmental Engineering, The Hong Kong Polytechnic University, Hong Kong, People's Republic of China

ABSTRACT

The acceleration of land desertification has led to an increasingly serious threat to the operation safety of tunnel entrance in the Gobi and desert regions by wind-sand flow, and it is urgent to study and enhance the running safety of train. Firstly, an ultrasonic anemometer is used to collect the characteristics of wind-sand flow at a tunnel entrance site in Xinjiang, China. Then, based on the Euler multiphase flow and the SST *k-w* model, the variation difference law of the train running at the tunnel entrance is revealed under the four inflow conditions of constant crosswind, constant wind-sand flow, pulsating crosswind and pulsating wind-sand flow respectively. Finally, the disturbance law of the solid wind barrier at the tunnel entrance on the wind-sand flow and the influence mechanism on the train's flow field structure and pressure are revealed. The results show that compared with other cases, the pulsating wind-sand flow has the most significant effect on the moving trains' aerodynamic loads (ALs), and the sand particles carried in the air cause the trains' ALs to fluctuate within 9.09%. The solid wind barrier has a significant disturbing effect on the wind-sand flow, and the lightweight sand particles follow the air flow over the top of the wind barrier and are not deposited on the embankment during a short period, and the wind-sand flow's impact on the HSTs is dramatically reduced. The wind barrier changes the HST's flow field, and the AL fluctuation of the train is sharply reduced. The maximum values of the head train's AL coefficients are reduced by 46.53–85.75%.

ARTICLE HISTORY
Received 31 August 2023
Accepted 1 November 2023

KEYWORDS
Wind-sand flow; High-speed train (HST); tunnel entrance; wind barrier; modeling

1. Introduction

As the development of Northwest China continues to progress, the high-speed rail lines (HSRLs) are being extended into areas of harsh environments such as the desert and Gobi. When the HSRL passes through the windy areas in Xinjiang (Deng et al., 2023; He et al., 2019; He & Li, 2020), the dust and debris on the ground under the strong crosswind are swept up to form the wind-sand flow that will jeopardize the operation safety of high-speed trains (HSTs). At the same time, wind-sand flow will bury infrastructure (such as tunnel and embankment) and affect their service life and function. During the operation of the HSTs, the wind-sand flow will impact the HST's surface, and in serious cases, it can penetrate the window glass of the HSTs, so plenty of wind barriers have been constructed along the HSRL from Lanzhou to Urumqi. However, the tunnel-embankment transition section is at the weak point of the HSRL section due to the rapid shear of the infrastructure. In the actual situation, sand still exists on the HSRL on the leeward side (LS) of wind barriers at the tunnel entrance. Therefore, it is of great significance to study the aerodynamic load (AL) changes of the carriage, the wear law of the carriage surface when the HST crosses the tunnel-embankment transition section under the wind-sand flow, as well as the movement and deposition law of the sand in the HSRL under the wind barrier's sheltering to ensure the safe operation of the HSTs.

At present, numerous researchers have conducted studies on the wind-sand flow's motion laws in Northwest China (Giudice & Preziosi, 2020; He et al., 2022; Horvat et al., 2021; Huang et al., 2018; Jiang et al., 2018; Tan et al., 2022, 2016; Wang et al., 2022b; Yao et al., 2012; Zhang et al., 2020). Wang et al. (2023) studied the motion pattern of sand in the Gobi stand in the strong wind area. The wind-sand hazard on sandy Gobi is more serious than that on gravel Gobi, and the sandy Gobi of Nanhu Lake is the main sand source of sand hazard on the rail

CONTACT Yi-Qing Ni ceyqni@polyu.edu.hk National Rail Transit Electrification and Automation Engineering Technology Research Center (Hong Kong Branch), Hong Kong, People's Republic of China; Department of Civil and Environmental Engineering, The Hong Kong Polytechnic University, Room Z105 1/F Z Block, Hung Hom Kowloon, Hong Kong 999077, People's Republic of China

from Hami to Lop Nor. Horvat et al. (2022) studied the sand deposition and erosion patterns around embankments under different wind speeds and directions and proposed an active sand blowing sand cleaning device. Huang et al. (2023) investigated the base shear force of low-rise buildings by different levels of sandstorms and found that the average shear force of the buildings increased as the level of the sandstorm increased. Tominaga et al. (2018) conducted wind tunnel experiments for erosion and deposition of cubic obstacles by wind-sand flow, which revealed the movement and deposition patterns of sand particles around cubic obstacles with wind speed and sand delivery, and verified that CFD can accurately predict the wind erosion patterns around cubic obstacles. Therefore, the function and safety of infrastructure such as embankment and track are affected under the wind-sand flow.

When the train runs in the desert and Gobi Beach, the AL of the train fluctuates significantly under the impact of crosswind, and the train surface is eroded and abraded by sand particles, even the train's laminated glass is broken (Arias-Cuevas et al., 2011; Carrascal et al., 2016; Faccoli et al., 2018; Hao et al., 2016; Kian et al., 2022; Li et al., 2021b; Zhang et al., 2021). Deng et al. (2019) studied the influence laws of wind barriers on the aerodynamic characteristics and dynamic response of the HSTs in a windy region of Xinjiang. Based on the discrete phase model (DPM) of computational fluid dynamics (CFD), Paz et al. (2015) evaluated the effects of suspended sand particles with different particle sizes and particle loads on the drag force and surface wear of the head train (HT). The accuracy of the DPM numerical simulation of sand impact on trains was verified by experiments. Deng et al. (2021) compared the dynamic response and damage rupture mechanism of laminated glass of the HST to the impact of wind-sand load through full-scale experiments. It was shown that the impact loading of sand particles caused the generation and extension of cracks in laminated glass, and with the increase of the diameter of sand particles the scratches of laminated glass extended dramatically and the laminated glass cracked rapidly. Based on the cohesive unit finite element model considering the covariant residual stress, Wang et al. (2022a) explored the effect of residual stress on the fracture mechanism and cracking pattern of laminated glass in trains, and found that an appropriate increase in the thickness of the polyvinyl butyral film can consume more kinetic energy of the impact to prevent the cracking of laminated glass. However, the above studies have only investigated the aerodynamic characteristics of trains under crosswinds or the wind-sand flow's impact on trains under stationary conditions, and few scholars have paid attention to the impact effect of wind-sand flow on moving trains.

The impact of strong wind-sand flow has serious harm to the HSTs and rail track facilities, many wind barriers have been built in desert and Gobi areas to prevent wind-sand flow, so as to ensure the safety of train operation (He et al., 2023; Li et al., 2019, 2021a; Masoud & Mohammad, 2013, 2018a, 2018b; Mehdipour & Baniamerian, 2019; Raffaele et al., 2021). Niu et al. (2022) compared the mitigation effects of single and double side wind barriers on nonlinear AL fluctuations of trains in a strong wind environment. The single-side wind barrier can effectively restrain the aerodynamic fluctuation of the train, and is an economical and efficient design scheme. Masoud et al. (2023) investigated the effect of different fence arrangements on the flow field structure around a high-speed train and analyzed the abrupt fluctuations of the aerodynamic force factor of the train. The results show that different fencing structures have considerable influence on the aerodynamic performance of the train. In order to determine the optimal design model of porous wind barriers, Masoud and Amir (2021) investigated the porousness level of the fence and the distance between the barriers based on the computational model of the 'lattice Boltzmann method' and the multi-objective genetic algorithm, and finally proposed the optimal design of the barriers. Based on the working principle of different types of solid barriers against wind-sand flow, Bruno et al. (2018a) linked the key geometric features of sand barriers to the sand blocking performance and introduced aerodynamic parameters as an approximate metric for their performance evaluation to provide guidance for sand barrier design. Sarafrazi and Talaee (2020) investigated the sand retention performance of a wind barrier on a HRSL during a sandstorm based on the Reynolds time-averaged turbulence model and the DPM. The results showed that the larger the diameter of sand particles, the smaller the effective sheltering distance behind the wind barrier, which is increased by increasing the wind speed. The optimal distance between the wind barrier and the track was finally determined. Bruno et al. (2018b) found that the sand particles carried by the wind often are deposited in the HSRLs, and the long-term sand retention performance of solid wind barriers fails to obtain the desired effect. The tunnel entrance's flow field is complex, and sand particles are easily deposited at the tunnel entrance, and when the train leaves the tunnel and encounters wind-sand flow, the operation safety of the train will be seriously deteriorated. However, few researchers have studied the disturbance characteristics of tunnel-embankment transition section wind barriers on wind-sand flow and the aerodynamic impact of wind-sand flow on the train under the condition of moving train.

In this study, based on the multiphase flow theory, the slip grid technique is adopted to realize the movement of the train, so as to obtain the characteristics of the sand deposition on the embankment on the LS of wind barriers at the tunnel entrance-embankment transition section; as well as the impacts of the wind-sand flow on the train surface and the transient aerodynamic evolution law of the carriage under the disturbance of wind barriers. Firstly, based on the wind-sand flow test of a tunnel-embankment transition section scenario in Xinjiang, the pulsating incoming wind speed data and sand samples are obtained, and the particle size distribution characteristics of the sand samples are obtained by sieving method. Then, a full-size 3D CFD dynamic model of train-tunnel-embankment-wind barrier is modeled based on the 'mosaic' grid technology of Fluent meshing, and the measured wind speed and sand parameters are loaded into the CFD model through the user-defined functions (UDF) program, which realizes numerical reconstruction of the wind-sand flow in the tunnel entrance of the HRSL. Finally, the deposition law of the wind-sand flow on the embankment under the disturbance of the wind barrier is analyzed, and the aerodynamic impact of the wind-sand flow on the train after the disturbance of the wind barrier is explored, as well as the evolution mechanism of the flow field behind it. The contribution of the paper is to propose a modeling method of wind-sand flow, which can provide guidance for the protection and control of wind-sand flow at the tunnel entrance of the HRSL.

2. Field test of wind field

2.1. Measuring point arrangement

The test site is located in a tunnel entrance of the Lanzhou-Xinjiang HSRL between Turpan and Hami (as shown in Figure 1). The tunnel-embankment transition section is located in the Baili wind zone, where the wind speed exceeds 30 m/s during the windy period, and the Lanzhou-Xinjiang HSRL runs geographically from east to west, with a counterclockwise deflection of about 5°. The tunnel entrance type of is the hat oblique, and a single solid wind barrier is built on the north side of the embankment. The wind barrier is 5.2 m high and 0.2 m thick.

As shown in Figure 2, a Gill Wind Master Pro ultrasonic anemometer (sampling frequency: 32 Hz) is

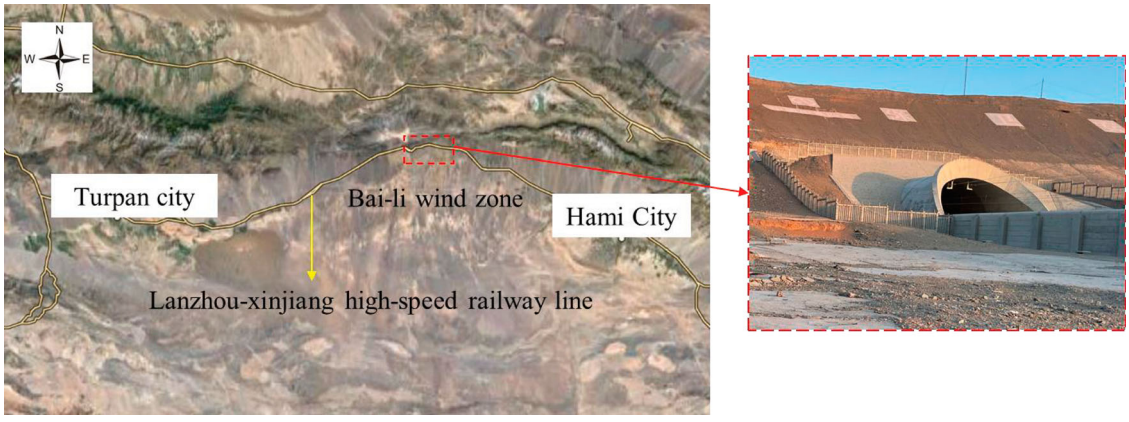

Figure 1. Location of field test.

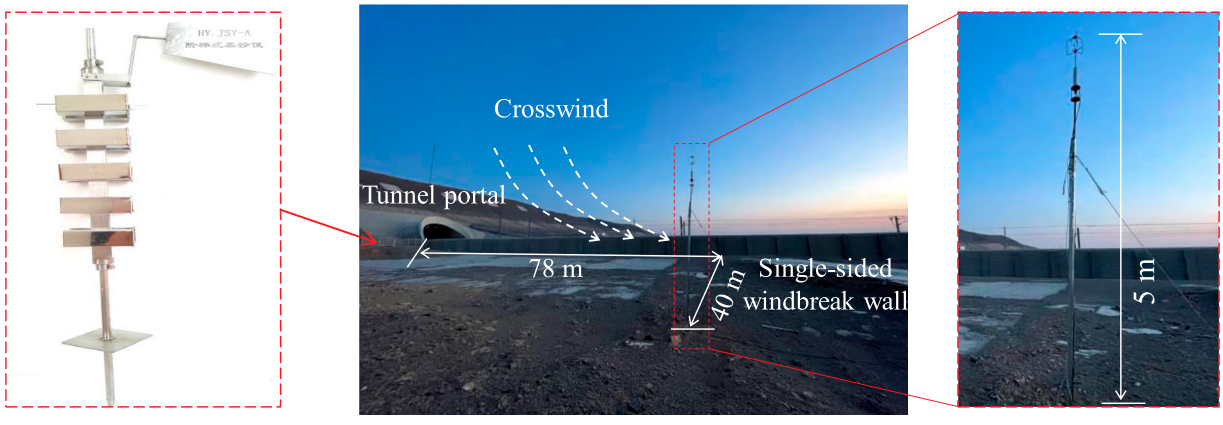

Figure 2. On-site layout of the measuring point.

Figure 3. Weighing and screening of sand particles.

installed on the windward side (WS) of the wind barrier. The anemometer is mounted on the solid wind barrier's WS by means of a wind tower, with the sensor height of the anemometer 5 m above the ground and a vertical distance of about 40 m from the wind barrier. The data acquisition system is the Campbell CR6.

2.2. Data processing

The study focuses on the horizontal crosswind impact effect. The original data collected by the ultrasonic anemometer include horizontal wind speed (U_h), horizontal wind Angle (θ) and vertical wind speed (U_w).

The HST running on a HSRL takes less than 3 s to exit the tunnel. Therefore, a time interval of 3 s is used to segment the samples, and the turbulence intensity of the samples is calculated according to the relevant formula (Yang et al., 2020).

As shown in Figure 2, a QN-JSY stepped sand accumulator is arranged at the tunnel entrance. As shown in Figure 3, electronic scales and national standard soil sieves are used for weighing and sieving of the sand particles in the laboratory of the High Speed Railway of Central South University.

2.3. Average wind speed and direction

The anemometer recorded 2 h samples of strong winds. Figure 4 shows the wind speed date of the measurement point, and Figure 5 shows the corresponding rose diagram of the wind direction.

As shown in Figure 4, the wind speed at the measurement point fluctuated dramatically during the two hours, with instantaneous wind speeds up to 32 m/s. The average wind speed at the station is 24 m/s (U_h) The wind speed of the U_w at the measurement point fluctuated at 0. In addition, as shown in Figure 5 that the wind direction of measurement point (U_h) is consistent and stable.

Table 1. Distribution of particle size range

Size (mm)	0–0.075	0.075–0.1	0.1–0.25	0.25–0.5	0.5–1	> 1
Weight (g)	0.26	3.37	9.95	39.98	22.76	9.63

When the wind speed exceeds 22 m/s, the wind direction is basically perpendicular to the HSRL, so the reconstruction of the wind-sand flow considers the wind speed on the horizontal plane as the vertical train direction and the other direction is perpendicular to the ground.

2.4. Turbulence intensity

Figure 6 shows the corresponding relationship between the turbulence intensity and the U_h. As shown in Figure 6, when the wind speed is low, the turbulence intensities are relatively dispersed, with the increase of wind speed, the turbulence intensity tends to a constant value of 0.04.

2.5. Characteristics of wind-sand flow

The sand particles collected by the sand accumulation instrument in the field experiment are weighed and screened in the laboratory. The sand particles are divided into [0-0.075], [0.075-0.1], [0.1-0.25], [0.5-1], [> 1] Six particle size ranges, the sand particle size distribution table is shown in Table 1, and the particle grading distribution curve is given as shown in Figure 7.

As shown in Table 1 and Figure 7: the total sand accumulation reaches 85.95 g. The particle size analysis of sand particles can better study the characteristics and sand deposition law of wind-sand flow. The light weight of small-sized sand particles makes it easy for them to be swept up by air flow and move, and easier to be deposited. The particle size range of sand particles is mainly concentrated in 0.1-2 mm, accounting for 95.78% of the total sand volume, of which the proportion

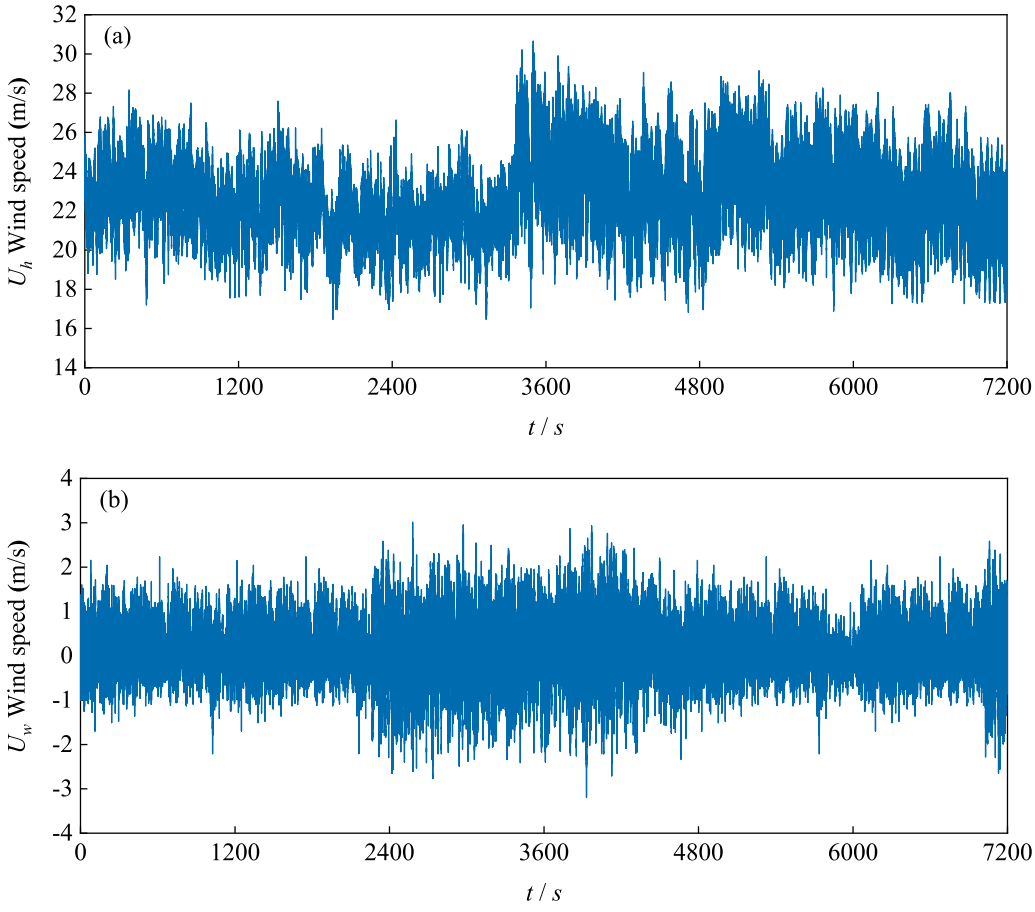

Figure 4. Instantaneous wind speed sample: (a) U_h, (b) U_w.

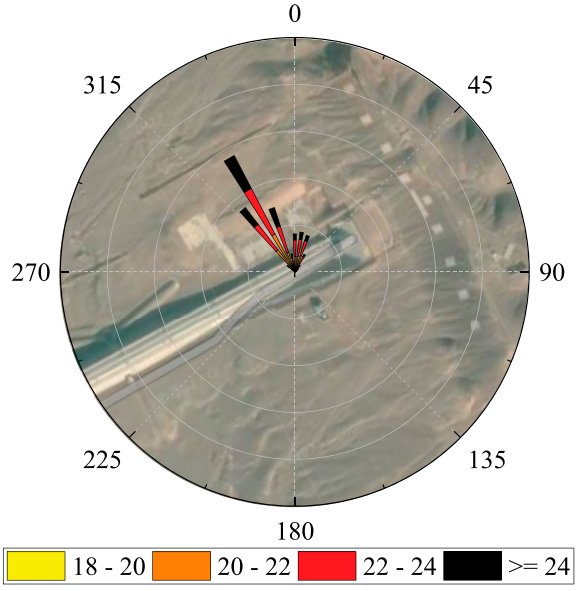

Figure 5. Wind rose diagram.

of 0.50 mm is as high as 46.52%. The particle size distribution of the sand particles showed normal distribution, and the sand particles were mainly medium and fine sand.

3. Methodology

3.1. Modeling scheme of wind-sand flow

3.1.1. Modeling of pulsating wind speed

The UDF program is compiled and loaded on the velocity-inlet boundary to establish a correspondence link in time between the measured date and the input date of the numerical model. The input time interval is 0.125s, the computational time step is 0.001s, and the wind speed values between the two input time points are interpolated using linear difference. To validate the reliability of the numerical simulation of pulsating wind speed, Figure 8 gives a comparison between the simulation to obtain the pulsating wind speed on the horizontal and vertical components (U_h and U_w) monitored by the velocity inlet and the corresponding input values. As shown in Figure 8, monitoring values at the velocity inlet are consistent with UDF inputs, indicating that the UDF procedure is reliable and the simulated pulsating incoming flow is consistent with the target wind field.

3.1.2. Reconstruction of sand particle

Xiong et al. (2011) gives the sand volume fraction corresponding to sand concentration under different intensity

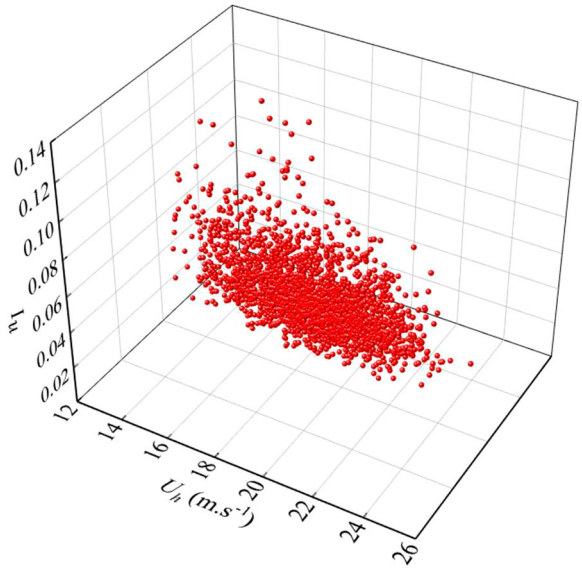

Figure 6. Turbulence intensity – wind speed.

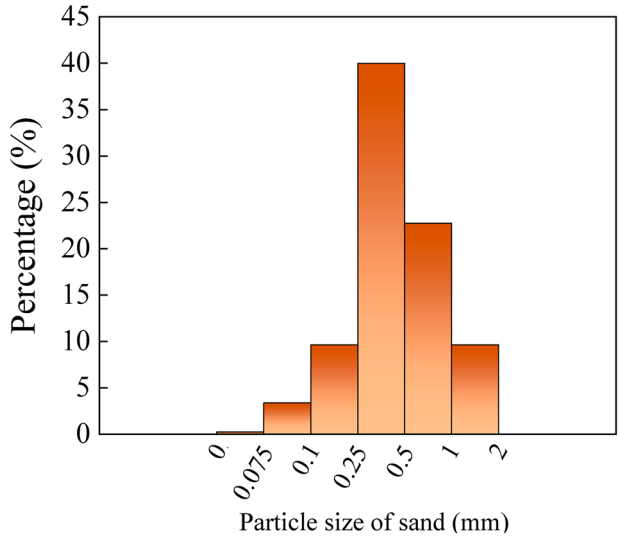

Figure 7. Proportion of sand size distribution.

of sandstorms. The linear difference method is also used to compile the sand volume fraction for different wind speeds into a UDF loaded into the velocity-inlet, so as to realize the real-time correspondence between wind speed and sand concentration. The measured sand particle size distribution is set in the sand phase of the Eulerian two-phase flow. When the crosswind speed is 24 m/s, the volume fraction of the sand phase is 3.12×10^{-8}ãĂĆ

3.2. Geometry and solution model

The geometrical dimensions of the computational model and the boundary conditions are given in Figure 9. The geometric dimensions of the model are dimensionless with reference to the actual dimensions of the CRH380B HST. The values of the length (L), width (W) and height (H) of a single carriage are 25, 3.27 and 3.89 m. The height and width of the computational domain of the tunnel entrance are 17.7 H and 31.4 W. The mountain wall is at an angle of 45° to the ground. The length of both the tunnel and the wind barrier section is 6.6 L. The tunnel is modeled as a standard two-line tunnel with a design speed of 350 km/h and a tunnel area of 100 m^2. The solid wind barrier at the tunnel entrance is 1.34 H and 0.055 W, with a porosity of 0. The pulsating wind speed and sand data of measured wind field are compiled into a UDF loaded into the velocity inlet. Symmetry boundary are used at the model's top. No-slip Wall is used for solid wall surfaces such as tunnels, floors, embankments, wind barriers and HST surfaces. Pressure-outlet is used for the tunnel outlet and incoming flow boundaries and at the opposing boundaries, respectively.

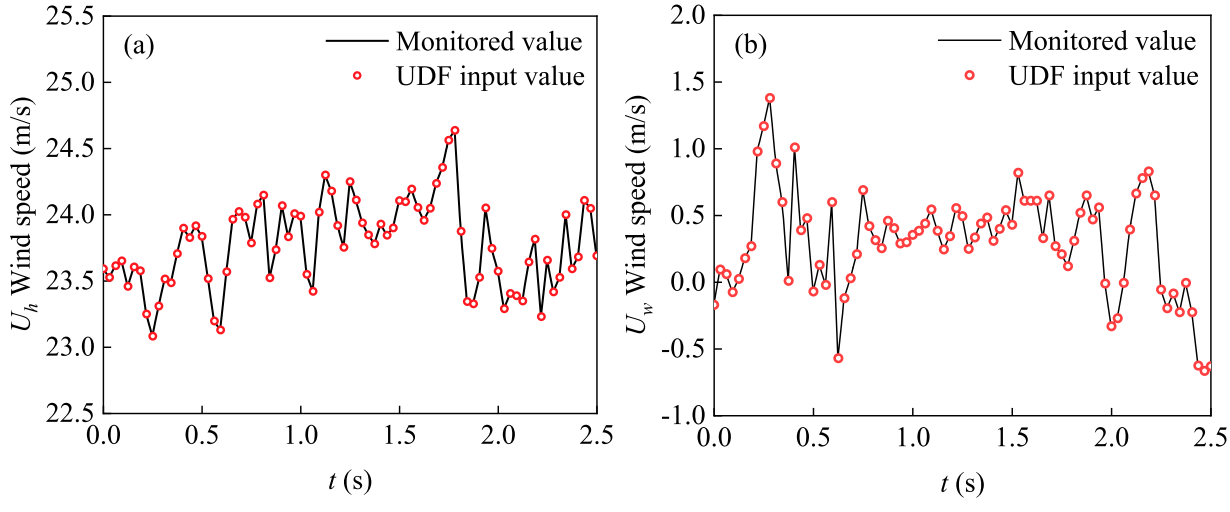

Figure 8. The pulsating wind speed monitored and the UDF input value: (a) U_h, (b) U_w.

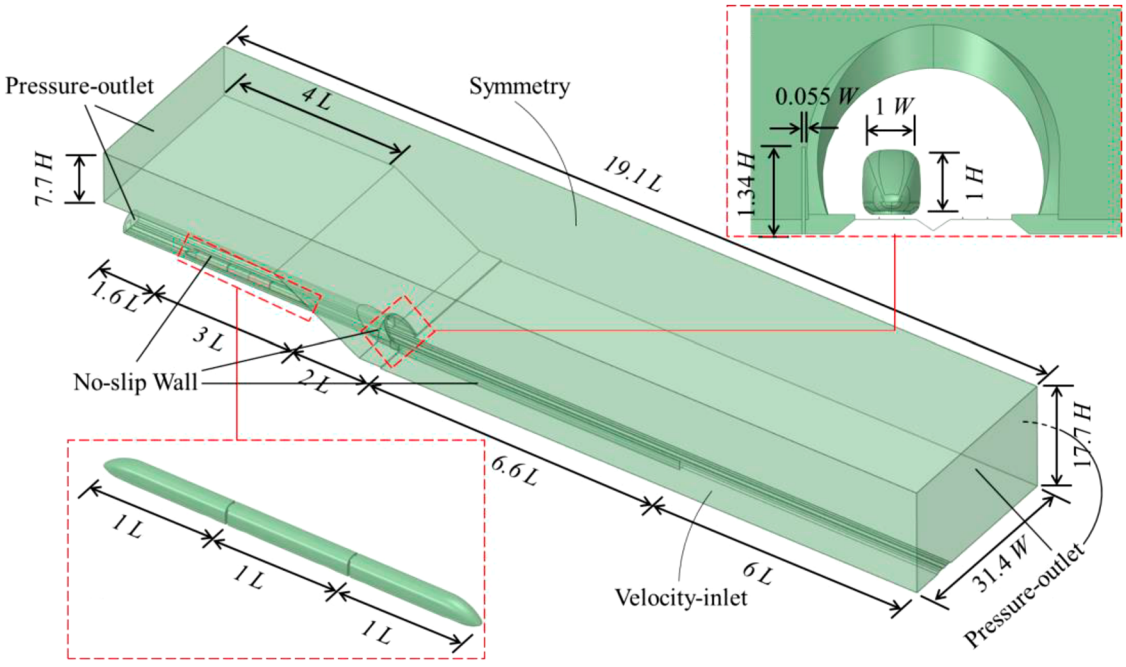

Figure 9. Information about the geometric model.

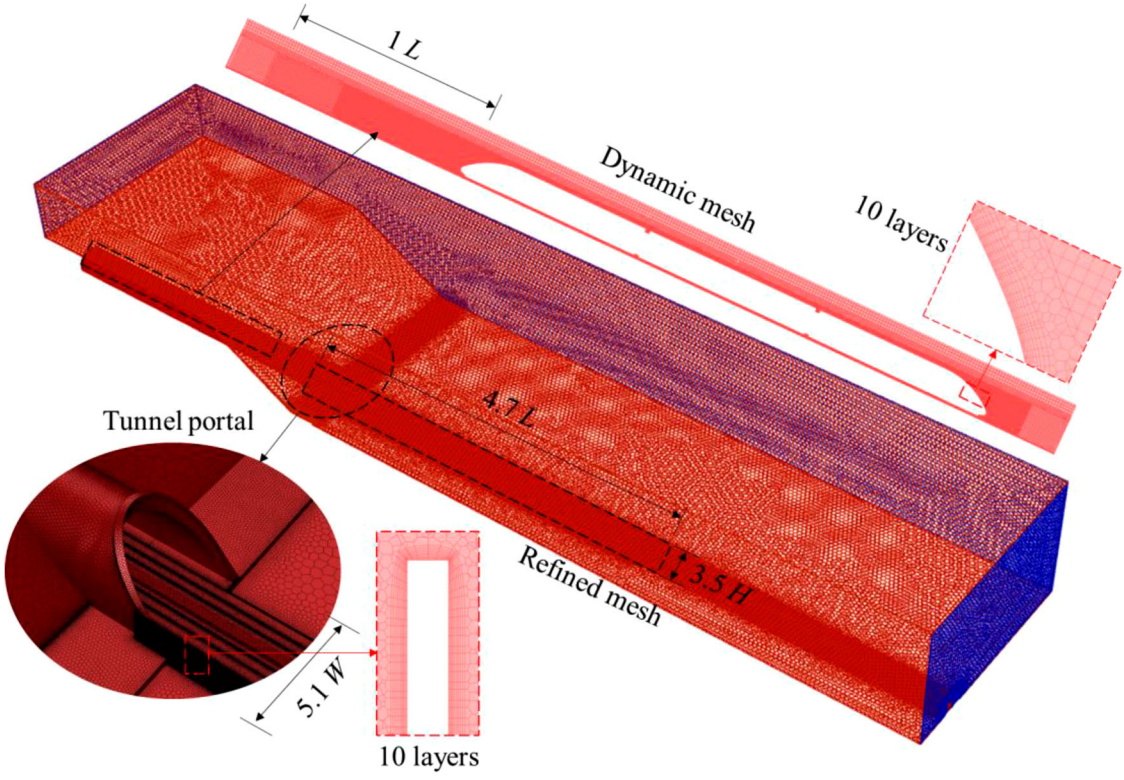

Figure 10. Overview of the grid.

3.3. Computational mesh

The grid details of the computational model are shown in Figure 10. The overall model is discretized using polyhedral grid cells using mosaic meshing technique of the Fluent meshing with a total number of grids of 36 million. The model adopts the layered moving mesh method to realize the relative motion of the HST, and Yang et al. (2020) provides a detailed description of the moving mesh method. Considering the complex evolution of the

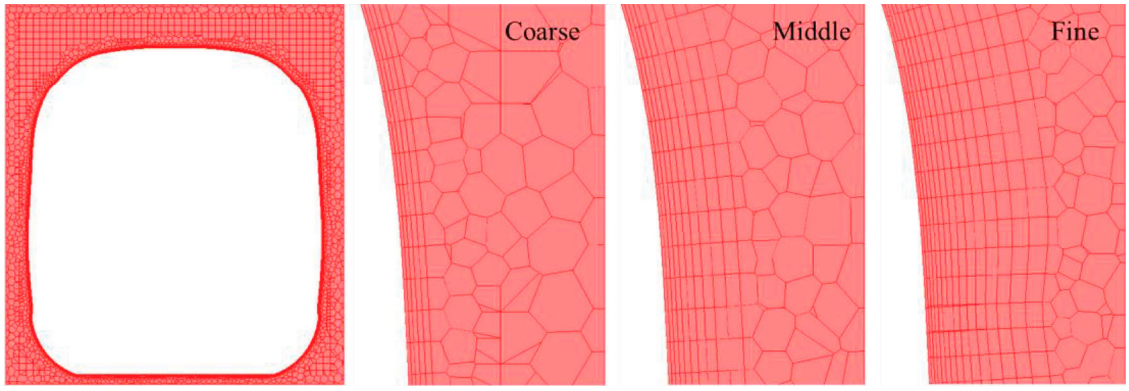

Figure 11. Different resolution grid.

flow field at the regions of the tunnel entrance, LS of the wind barrier and tail train (TT), the grid of the region needs to be refined. The grid size of the refined region at the tunnel entrance and the LS of the wind barrier is limited to 4×10^{-3} L, and the extent of the region is 2.3 L, 5.7 W and 2.3 H. 10 layers of surface are generated at the tunnel wall and the wind barrier wall. The response of the HST are the focus of the study, so the grids around the HST are refined. The grid size of the HST surface is 5-$\times 10^{-4}L$, and 10 layers are also generated on the HST surface, with the thickness of the first grid layer being $5 \times 10^{-4}L$ ($y^+ < 10$). The computational model is solved transiently using the SST k-w turbulence model with 0.001s time step. Therefore, the model is computed at the supercomputer center in Wuxi, and each model takes 10 days to complete using 144 cores.

3.4. Mesh sensitivity study

The fine grid can get a more accurate solution result, especially in the study of the train dynamic mesh refinement area plays a crucial role in the whole calculation process. Therefore, the grid independence verification is carried out for the surface grid and the attached surface layer of the train, and the three encryption schemes for the attached surface layer are shown in Figure 11, with the total grids of 30, 38 and 46 million representing the coarse, medium and fine resolution levels, respectively. Using the 24 m/s crosswind and sand volume fraction of 3×10^{-8} as an example, Figure 12 shows the corresponding lateral force of the three grid schemes.

As shown in Figure 12, the number of surface layers has a significant effect on the HT's lateral force coefficient (C_z), especially in the tunnel entrance and the wind barrier section. Compared to the 46 million grid model, the maximum difference in lateral force between the 30 and 38 million grid models is 12.4% and 2.9%, respectively. The computation times for the 30, 38,46 million grids are 7, 10 and 15 days, respectively. Therefore, the medium

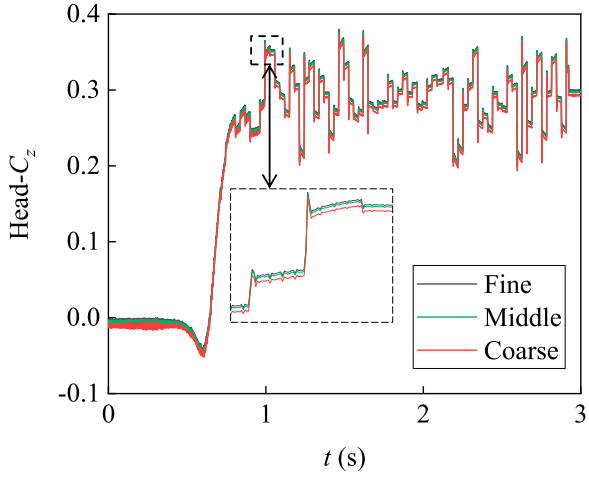

Figure 12. Lateral force values of the three resolution grids.

resolution model is able to guarantee accuracy having less number of grids and the 38 million grid encryption scheme is reasonable and efficient.

3.5. The cases considered

As shown in Table 2, 5 cases are considered in the study. The effects of sand particles of the air on the HST's aerodynamic characteristics when it exits a tunnel entrance are investigated for the C1 and C2 under the effect of a crosswind with a constant 24 m/s. The natural crosswind at the tunnel entrance is the turbulent wind with complex pulsation components. Therefore, C3-C4 investigates the influence of sand particles on the HST's aerodynamic characteristics and the sand movement law under the turbulent wind. Finally, based on the measured wind speed data in the field, C5 explores the disturbance pattern of the wind-sand flow by wind barrier and the change of ALs of the HSTs.

3.6. CFD validation

A wind-train-tunnel-embankment model is modeled by reference to the tunnel-embankment transition section

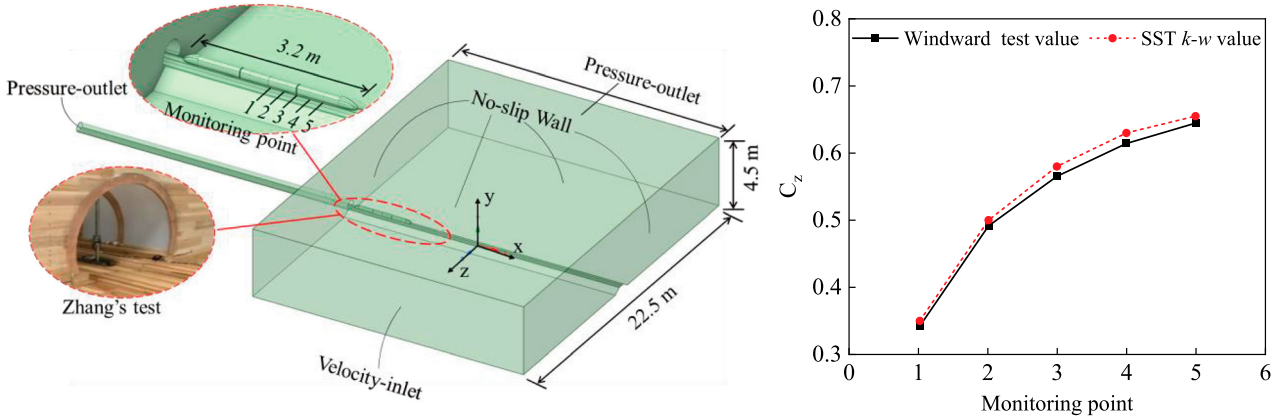

Figure 13. Wind-train-tunnel-embankment dynamic model and lateral force values.

Table 2. Calculation cases considered in the study.

Case	Incoming flow	Wind speed	Turbulence intensity	Wind barrier
C1	Constant wind	24	0	Without
C2	Pulsating wind	Fluctuations up and down 24	0.04	Without
C3	Constant wing-sand	24	0	Without
C4	Pulsating wind-sand	Fluctuations up and down 24	0.04	Without
C5	Pulsating wind-sand	Fluctuations up and down 24	0.04	Exist

experiments in the XNJD-3 atmospheric boundary layer wind tunnel (1:20 scale) at Southwest Jiaotong University (shown in Figure 13). The type of boundary conditions and turbulence model used are consistent with the case in the paper. A steady crosswind of 8 m/s is added in the wind tunnel to impact a stationary train at the embankment section to monitor the HST's C_z. Simulation results are validated with the experimental datas of Zhang et al. (2019). To make the dates comparable, the ALs are dimensionless. As shown in Figure 13, the C_z of train is simulated by the SST k-w model is in basic agreement with the wind tunnel dates, with the difference within 7%. Therefore, the wind-train-tunnel-embankment model based on the SST k-w in the paper is considered reliable.

4. Results and discussions

4.1. Aerodynamic loads of the moving train under four inflow conditions

The ALs of the carriages are calculated by using the unit surface pressure integration method and are dimensionless (i.e. C_z, the lift coefficient C_y, the roll moment coefficient C_{mx}, the yaw moment coefficient C_{my}, and the pitch moment coefficient C_{mz}). Table 3 counts the peak values of the five AL coefficients for the three carriages during the HST exiting the tunnel and when the HST is fully running on the open line. According to Niu et al. (2022), the standard deviation can quantitatively characterize the AL fluctuations of the HST and indirectly obtain the vortex shedding frequency around the HST. In the study, the AL coefficients of the three carriages are processed to obtain the standard deviation as shown in Table 4.

During train operation, its ALs are largely influenced by the local flow around the train, and the degree of fluctuation of the ALs is caused by the oscillation of the incoming wind speed. However, when there are sand particles on the ground, sand particles are wrapped in the HST's airflow to form the wind-sand flow. The dynamic response of the train to the wind-sand flow will be more complicated under the interaction of airflow and sand particles. Figure 14 gives the five AL coefficients of the HT, middle train (MT) and TT under four incoming flows.

Comprehensive analysis of Figure 14, Table 3 and Table 4 shows that:

The HST's AL coefficients fluctuate drastically during the HST exiting the tunnel, especially for the HT. When the wind speed is constant, the five ALs of the carriages are maintained at the peak level and fluctuate steadily on the embankment. When the air contains sand particles, it takes energy for the air to drive the sand particles into motion, resulting in a decrease in the crosswind speed. As a result, the maximum values of the coefficients of C_z, C_{mx} and C_{my} of the HT are reduced by 0.004 (1.27%), 0.001 (9.09%) and 0.002 (0.40%), respectively, when the train exits the tunnel under the wind-sand flow. However, the sand movement leads to the change of the HST's flow field, and the C_y and C_{mz} of the HT increase by 0.017 (4.93%) and 0.002 (1.39%). The HST's running process is more bumpy and passenger comfort is reduced.

However, the actual natural wind field is often turbulent wind, and the HST's external flow field structure

Table 3. Maximum value of the AL coefficient of the three carriages.

		OUT				Crosswind			
	Carriage	C1	C2	C3	C4	C1	C2	C3	C4
Head	Max C_y	0.345	0.335	0.362	0.351	0.328	0.325	0.340	0.339
	Max C_Z	0.316	0.363	0.312	0.363	0.308	0.379	0.301	0.379
	Max C_{mx}	0.011	0.018	0.010	0.018	0.010	0.019	0.019	0.020
	Max C_{my}	0.502	0.501	0.500	0.504	0.345	0.381	0.347	0.389
	Max C_{mz}	0.144	0.139	0.146	0.144	0.119	0.124	0.122	0.127
Middle	Max C_y	0.267	0.267	0.277	0.272	0.255	0.251	0.261	0.259
	Max C_Z	0.152	0.235	0.146	0.228	0.149	0.236	0.139	0.227
	Max C_{mx}	0.012	0.022	0.012	0.022	0.011	0.023	0.011	0.023
	Max C_{my}	0.159	0.174	0.144	0.169	0.051	0.063	0.049	0.058
	Max C_{mz}	0.014	0.014	0.012	0.014	−0.023	−0.024	−0.024	−0.026
Tail	Max C_y	0.198	0.196	0.216	0.210	0.188	0.189	0.204	0.204
	Max C_Z	0.086	0.160	0.085	0.160	0.009	0.097	−0.001	0.087
	Max C_{mx}	0.006	0.016	0.006	0.015	0.001	0.012	0.000	0.010
	Max C_{my}	0.287	0.280	0.272	0.270	0.265	0.276	0.263	0.277
	Max C_{mz}	0.020	0.013	0.017	0.018	−0.102	−0.101	−0.113	−0.111

Table 4. Standard deviation values of the AL coefficients for three carriages.

		OUT				Crosswind			
	Carriage	C1	C2	C3	C4	C1	C2	C3	C4
Head	Δ C_y	0.143	0.139	0.149	0.146	0.001	0.007	0.002	0.007
	Δ C_Z	0.142	0.143	0.141	0.143	0.002	0.035	0.001	0.035
	Δ C_{mx}	0.005	0.006	0.005	0.005	0.000	0.004	0.000	0.004
	ΔC_{my}	0.196	0.194	0.198	0.197	0.003	0.014	0.001	0.014
	Δ C_{mz}	0.074	0.072	0.078	0.077	0.001	0.003	0.001	0.003
Middle	Δ C_y	0.093	0.091	0.097	0.096	0.002	0.007	0.002	0.007
	Δ C_Z	0.057	0.059	0.053	0.056	0.001	0.036	0.001	0.037
	Δ C_{mx}	0.004	0.005	0.004	0.005	0.000	0.005	0.000	0.005
	ΔC_{my}	0.047	0.047	0.046	0.046	0.001	0.005	0.002	0.006
	Δ C_{mz}	0.064	0.063	0.068	0.067	0.003	0.003	0.003	0.004
Tail	Δ C_y	0.068	0.067	0.074	0.074	0.002	0.007	0.002	0.008
	Δ C_Z	0.026	0.030	0.026	0.029	0.001	0.036	0.001	0.036
	Δ C_{mx}	0.003	0.003	0.002	0.003	0.000	0.004	0.000	0.004
	ΔC_{my}	0.091	0.091	0.087	0.087	0.002	0.013	0.001	0.013
	Δ C_{mz}	0.064	0.063	0.069	0.068	0.002	0.003	0.002	0.003

changes significantly under the turbulent wind. Therefore, when the incoming flow is turbulent wind, the HST's AL not only changes abruptly in the infrastructure switching situation, but also the HST's ALs fluctuates dramatically in the embankment section with the change of the incoming wind speed. Compared to the pulsating wind-sand flow condition, the maximum value of the five AL coefficients of the HT under constant wind-sand flow decreases by 0.020 (60.61%), 0.173 (96.11%), 0.022 (95.65%), 0.087 (91.58%), and 0.013 (54.17%), respectively. The standard deviations of the HST's AL coefficients for the constant wind-sand flow are all below 0.03. However, the standard deviations of the HST's AL coefficients for the pulsating wind-sand flow are all more than 0.03, and it is noteworthy that the standard deviation of the C_z coefficient is as high as 0.36, and the strength of the leeward vortex shedding of the HST under the turbulent wind is significantly changed. Therefore, the change of wind speed in the pulsating wind field plays a significant influence on the HST's flow field characteristics.

When the incoming flow are pulsating wind, and sand particles are present in the airflow, the change of the HST flow field is more complicated. Compared with the constant wind-sand flow (C3), the variation of the ALs of the HST increased slightly. In the tunnel entrance section, the maximum values of the five AL coefficients of the HT increased by 0.011 (3.02%), 0.001 (0.24%), 0.001 (4.55%), 0.007 (1.24%) and 0.017 (6.01%), respectively. In the embankment section, the maximum values of the five AL factors for the HT increased by 0.001 (3.13%), 0.004 (2.27%), 0.001 (4.55%), 0.002 (2.13%) and 0.001 (4.35%), respectively.

In summary, the HST's AL coefficients have the largest change amplitude under pulsating wind-sand flow, and the HST's operation safety is under the greatest threat. Compared with the constant wind-sand flow, the pulsating wind-sand flow will cause the fluctuation of the AL of the HST, the maximum difference of the AL coefficients fluctuation is 96.11%, the standard deviation of the C_z coefficient has the largest change. The

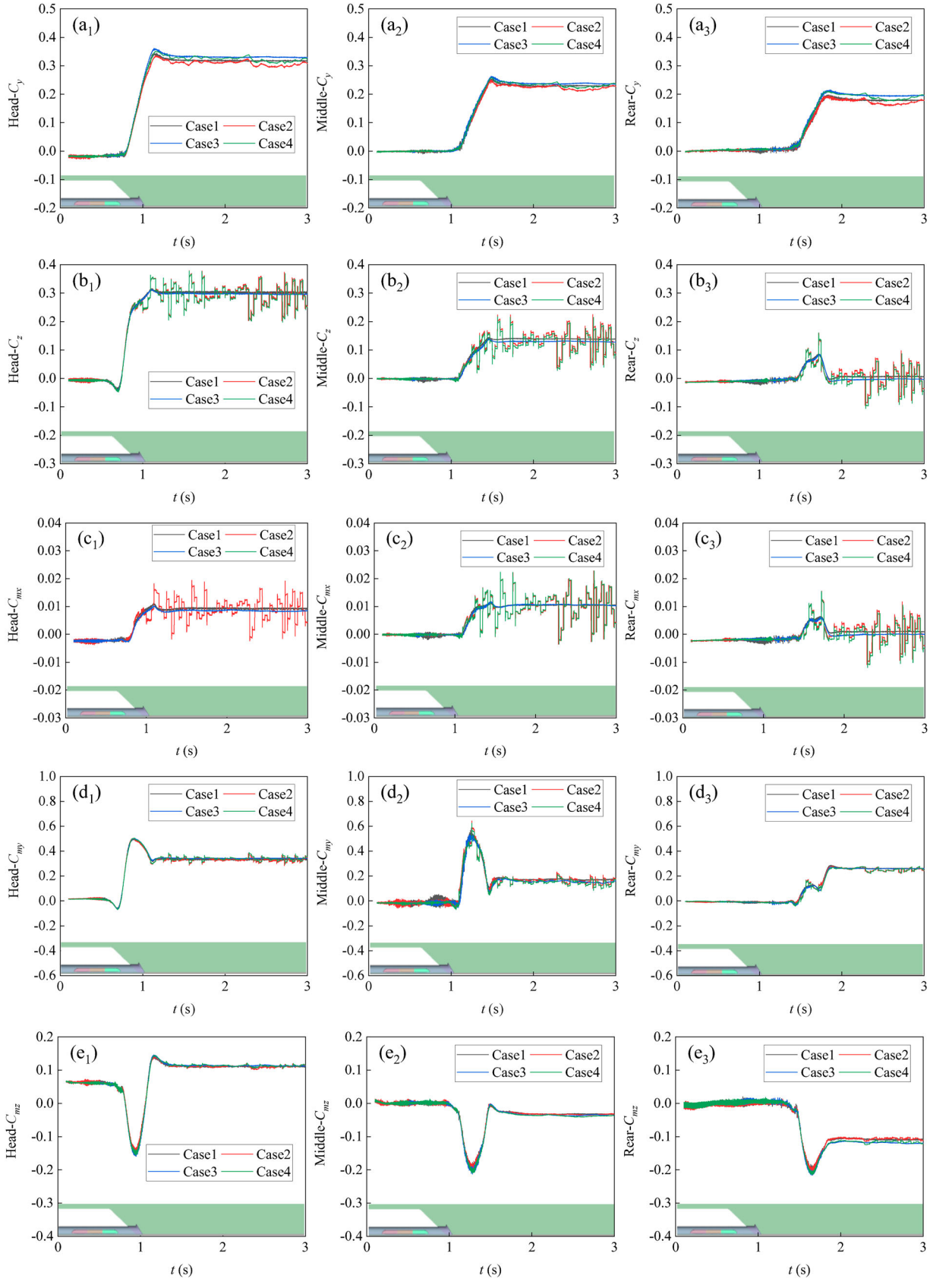

Figure 14. Five AL coefficients: (a) C_y, (b) C_z, (c) C_{mx}, (d) C_{my} and (e) C_{mz}.

intensity of vortex shedding on the HST's LS under the impact of pulsating wind-sand flow fluctuates dramatically, which in turn causes the HST's compartment body to agitate. When sand particles are wrapped in the air, it will cause the HST's ALs to change within 9.09%.

4.2. Aerodynamic loads of the moving train under wind barriers

In practice, wind barriers are constructed on the WS of the HSRL in windy areas to resist the impact of high-speed crosswinds on HSTs. The wind barriers reduce the fluctuation of the HSTs' ALs of and protect the operation safety of the HSTs. Figure 15 gives the AL coefficients when the HST leaves the tunnel under the pulsating wind-sand flow (with or without windbreaks), and the maximum values and standard deviations of the AL coefficients of the three carriages are shown in Table 5.

As shown in the Figure 15 and Table 5:

The fluctuation of the HST's AL decreases sharply when the wind barrier is installed at the tunnel entrance, and the HST exits the tunnel and operates in the pulsating wind-sand flow. The maximum values of C_y, C_z, C_{mx}, C_{my} and C_{mz} of the HT are reduced by 0.301 (85.75%), 0.234 (64.46%), 0.009 (50.00%), 0.410 (81.35%) and 0.067 (46.53%), respectively. The wind barrier changed the HST's flow field, and the C_z and C_{my} of the train changed from positive Z direction (incoming flow direction) to negative Z direction. The wind barrier reduces the impact of wind-sand flow on the HST, the frequency and intensity of vortex shedding on the LS of the HST are decreased, and the standard deviation of the train's AL coefficients are significantly reduced. The standard deviation of the C_y, C_z, C_{mx}, C_{my} and C_{mz} of the HT are reduced by 0.301 (85.75%), 0.234 (64.46%), 0.009 (50.00%), and 0.41 (81.35%), and 0.067 (46.53%), respectively.

4.3. Flow field structure

In order to study the effect of wind barrier on the evolution of transient vortex structures around the HST, the HST's flow field and vortex structures at the tunnel entrance-embankment segments under the impact of pulsating wind-sand flow are given in Figure 16 and Figure 17. The isosurfaces of the vortex structures are generated based on the Q-criterion and colored with a dimensionless velocity ($U_r = 35.7$ m/s).

As shown in Figure 16: When the HST leaves the tunnel, under the impact of pulsating wind-sand flow, the airflow forms a vortex above the LS of the carriage, which leads to the train's C_z, C_{my} and C_{mz} to grow in a negative direction first. Many separating vortices exist on the HST's LS under the impact of pulsating wind-sand flow, and these vortices are the main cause of aerodynamic fluctuations of the HST. The coupling of HST's wind and pulsating wind-sand flow leads to the development of vortices from the HT to the TT gradually increasing and moving away from the train. As a result, the HST's ALs grow from the negative direction to the positive direction. Since the wind speed of the wind-sand flow is fluctuating in real time, the HST's flow field will also change continuously, resulting in the ALs of the HST fluctuating with the change of wind speed.

Wind barriers can reduce the violent changes in the HST's flow field structure, minimize the fluctuation of the ALs of the HST and thus ensure the safety of the train. When a wind barrier is installed at the HSRL, the wind-sand flow bypasses the tunnel entrance and evolves into vortex structures on both the WL and LS of the HST. The vortex structure on the LS of the HST is larger and shifted downward compared to the one without a wind barrier (C4). Due to the formation of vortex structures on both sides of the HST, both sides of the carriage are subjected to negative pressure at the same time, which partially offsets the pressure difference of the carriage and thus reduces the ALs on the HST.

As shown in Figure 17: A large detached vortex structure can be captured at the tunnel entrance when the HST operates on the HSRL without wind barrier. Two large vortex structures are detached from the HST's LS under the impact of pulsating wind-sand flow, a longitudinal vortex is continuously detached from the streamlined nose of HT, and the other one develops from the middle of the HT toward the MT gradually increasing and vortex detachment. The streamlined nose of HT, the WS and the roof of the HST all become positive pressure, and the LS of the HST becomes negative pressure. Due to the existence of the pressure difference of the carriage, the HST as a whole is subjected to C_z and C_{my} under the incoming flow. While the HST runs on the embankment with wind barrier, the longitudinal vortex structure on the HST's LS disappears. Striped vortex structures are captured around the top of the wind barrier, and multiple separated vortex structures are captured on the HST's WS, especially on the TT's WS. The presence of a single-side wind barrier significantly reduces the strength and size of the vortices around the HST.

4.4. Cross-sectional pressure of the train

To analyze the influence law of the wind barrier on the HST's aerodynamic pressure, Figure 18 gives the pressure distribution in the cross section of the carriages (middle section of the HT, MT and TT) when the HST is running

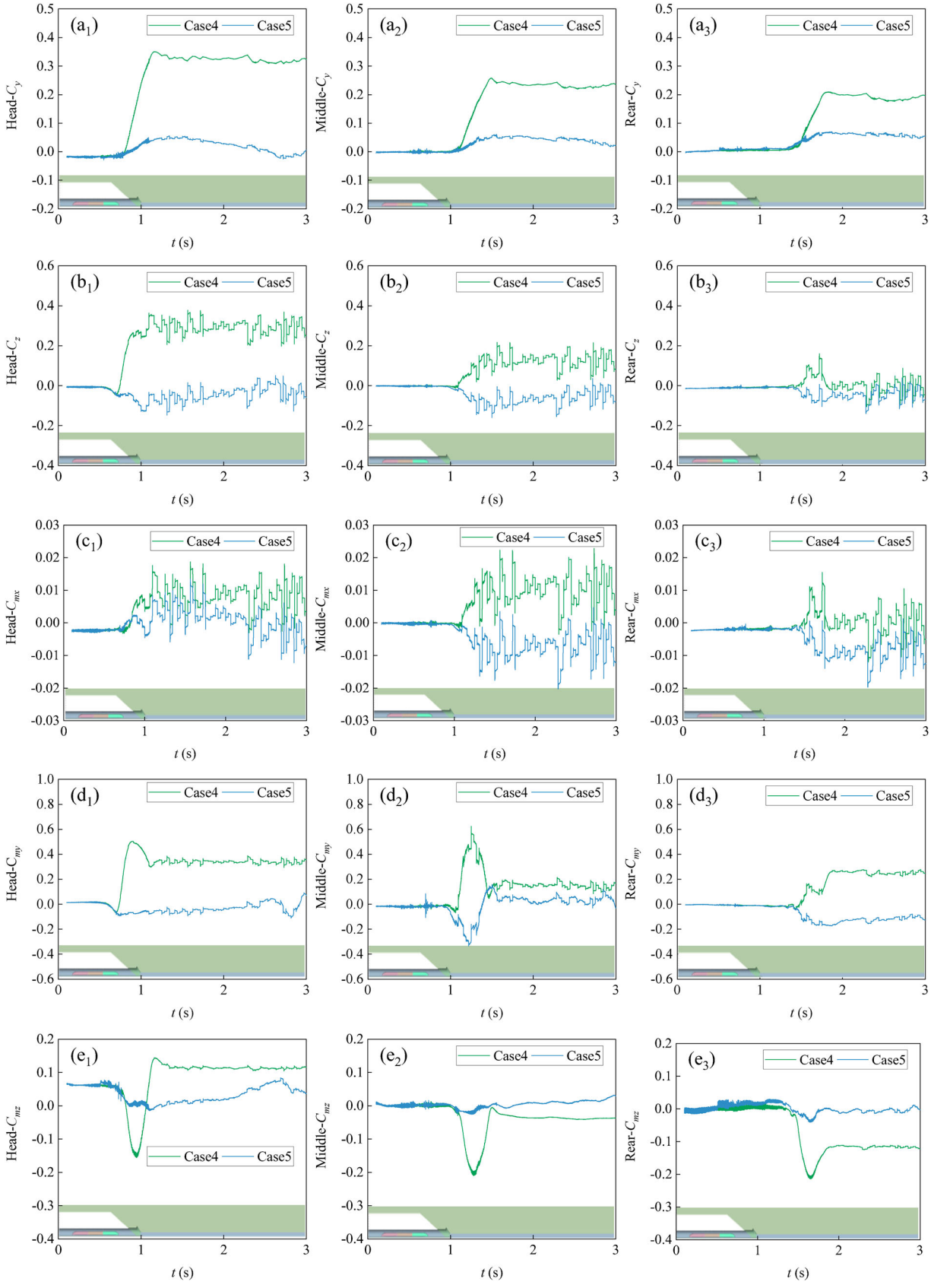

Figure 15. Five AL coefficients: (a) C_y, (b) C_z, (c) C_{mx}, (d) C_{my} and (e) C_{mz}.

Table 5. Maximum and Standard deviation values of the AL coefficients of the three carriages.

		OUT		Crosswind			OUT		Crosswind	
	C4	C5	C4	C5	C4		C5	C4	C5	
Head	Max C_y	0.351	0.050	0.339	0.056	ΔC_y	0.146	0.025	0.007	0.023
	Max C_Z	0.363	0.129	0.378	0.147	ΔC_Z	0.143	0.036	0.035	0.036
	Max C_{mx}	0.018	0.009	0.019	0.013	ΔC_{mx}	0.005	0.003	0.004	0.004
	Max C_{my}	0.504	0.094	0.389	0.111	ΔC_{my}	0.197	0.040	0.014	0.039
	Max C_{mz}	0.144	0.077	0.127	0.084	ΔC_{mz}	0.077	0.030	0.003	0.022
Middle	Max C_y	0.272	0.064	0.259	0.059	ΔC_y	0.096	0.021	0.007	0.010
	Max C_Z	0.228	0.006	0.227	0.039	ΔC_Z	0.056	0.041	0.037	0.034
	Max C_{mx}	0.022	0.003	0.023	0.005	ΔC_{mx}	0.005	0.015	0.005	0.016
	Max C_{my}	0.169	0.043	0.058	0.032	ΔC_{my}	0.046	0.100	0.006	0.025
	Max C_{mz}	0.014	0.017	−0.026	0.033	ΔC_{mz}	0.067	0.033	0.004	0.032
Rear	Max C_y	0.210	0.070	0.204	0.068	ΔC_y	0.074	0.023	0.008	0.005
	Max C_Z	0.160	0.007	0.087	0.039	ΔC_Z	0.029	0.022	0.036	0.031
	Max C_{mx}	0.015	0.001	0.010	0.001	ΔC_{mx}	0.003	0.003	0.004	0.004
	Max C_{my}	0.270	0.004	0.277	−0.078	ΔC_{my}	0.087	0.061	0.013	0.015
	Max C_{mz}	0.018	0.030	−0.111	0.012	ΔC_{mz}	0.068	0.015	0.003	0.006

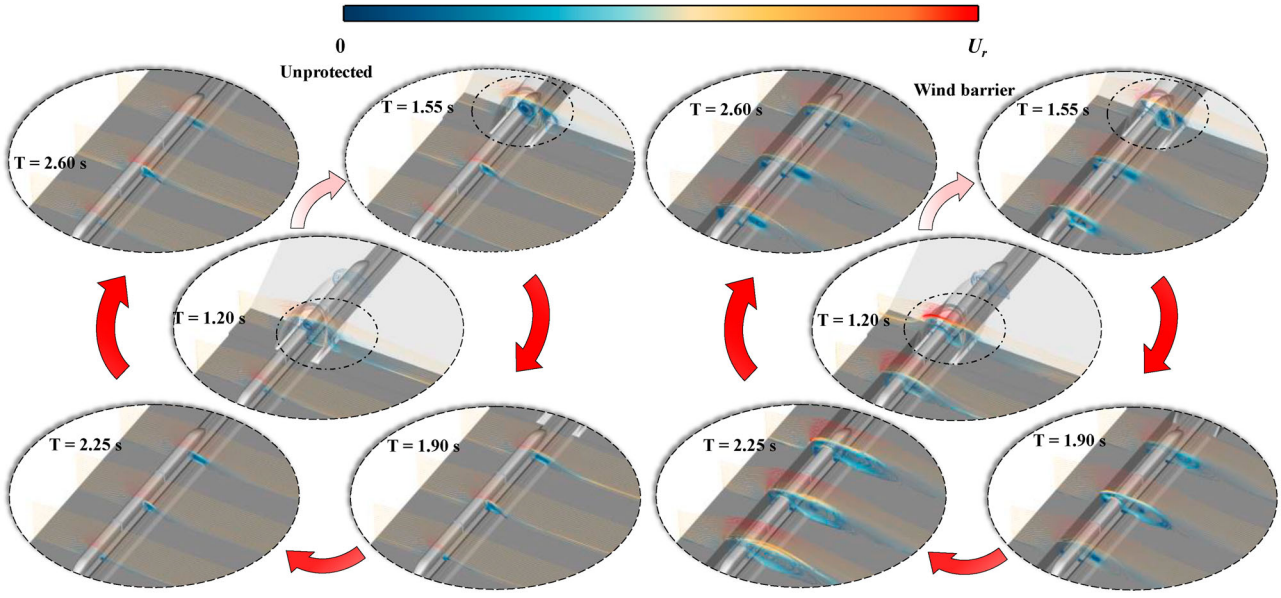

Figure 16. Evolution of the HST's flow field structure.

on the embankment under the impact of the pulsating wind-sand flow, $P_r = 300$ Pa.

As shows in Figure 18, under the impact of pulsating wind-sand flow, the HT's WS is subject to positive pressure and the roof is subject to negative pressure. Therefore, the HT is subjected to C_z in the direction of incoming flow and vertical upward C_y. The WS and the junction of the MT is under positive pressure, and the roof and the junction of the roof and the WS of the MT is under negative pressure. In addition, due to the existence of the vortex on the LS of the MT, the MT is subject to the greatest negative pressure. The positive on the TT is minimized. When the WS of the HSRL is equipped with a wind barrier, the wind barrier is subjected to aerodynamic pressure from the pulsating wind-sand flow, and the carriages' surfaces are subjected to negative pressure and the negative pressure decrease. The change in the HST's pressure distribution leads to the corresponding shift in the HST's ALs, and all five ALs are reduced. However, there are multiple separating vortex structures at the TT's top, and the top of the compartment body of the tail car is negatively pressurized and subjected to upward pulling force, and the TT's C_y and C_{mz} are larger than that of the HT and the MT.

4.5. Sediment characteristics of sand

In addition to the effect of wind-sand flow on the aerodynamic response of the HST, sand particles will be deposited and attached to the embankment and HST surface. The presence of sand particles affects the service life and operational safety of the HST, so the movement and deposition pattern of the sand particles are very important. After the wind-sand flow passes through the wind

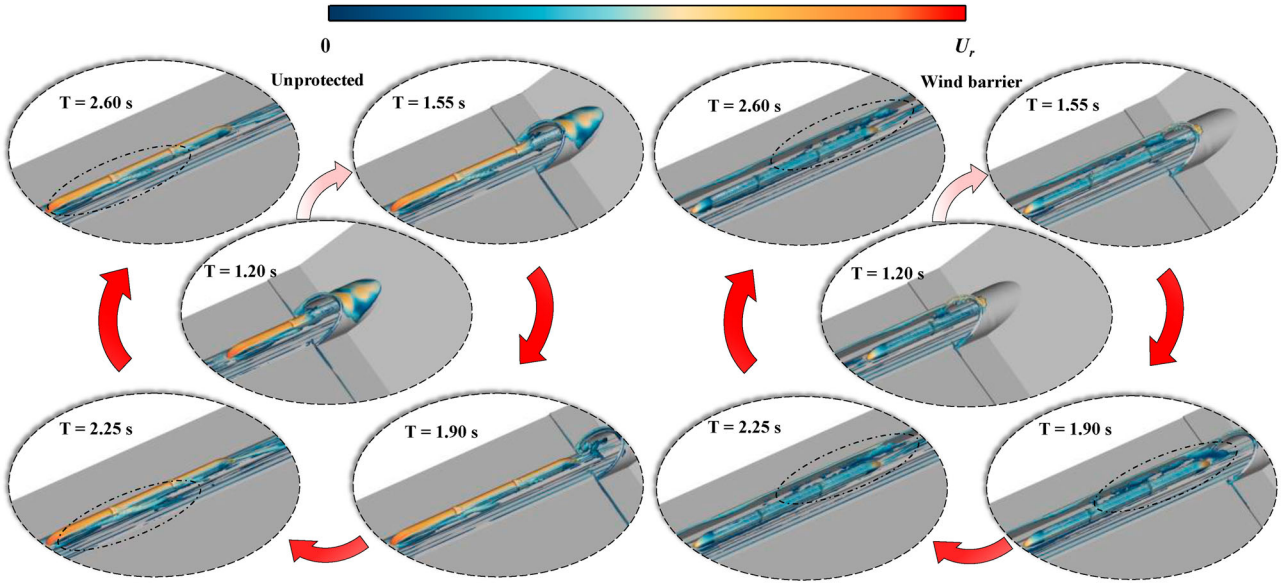

Figure 17. Evolution of the vortex structure around the HST.

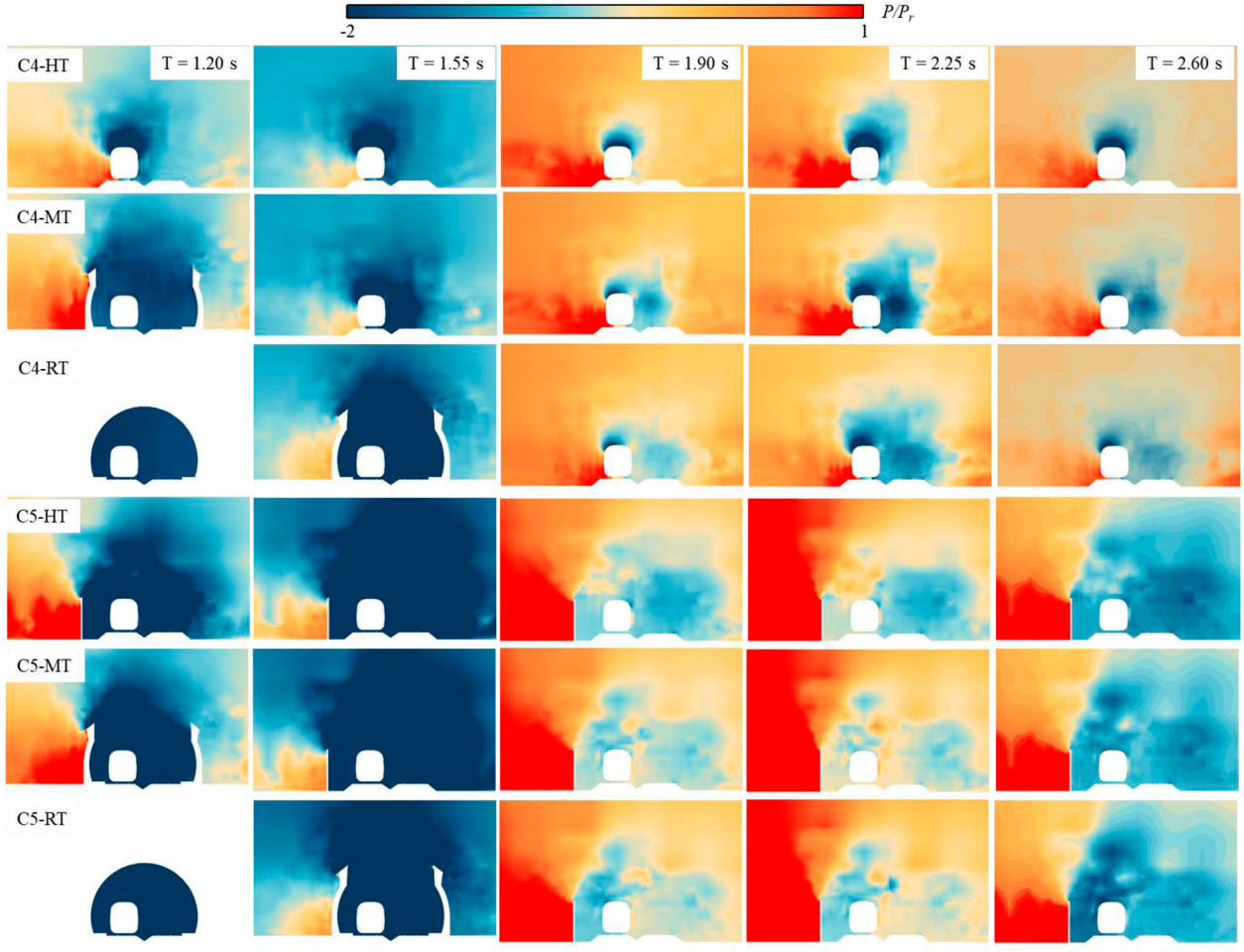

Figure 18. Cross-sectional pressure distribution of the HST.

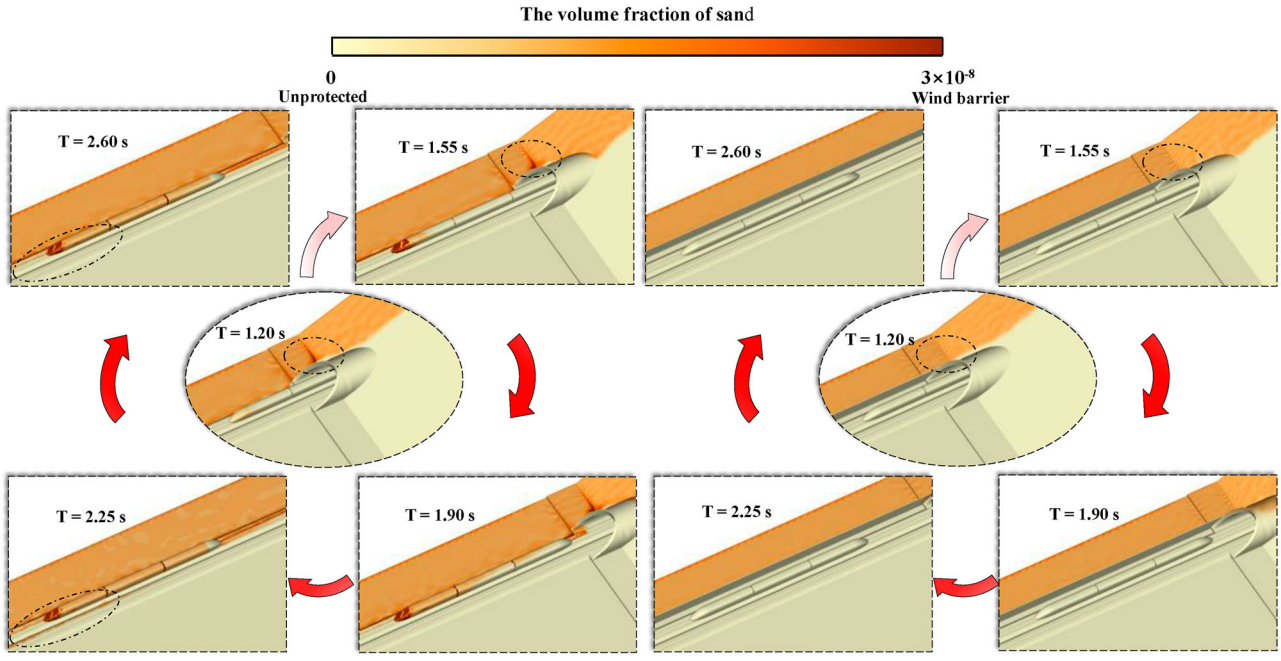

Figure 19. 3D volume fraction distributions of the sand phase.

barrier, the flow field structure behind the wind barrier and around the HST is changed, which is conducive to the improvement of the overturning stability of the HST and has a significant protective effect on the safe operation of the HST. The wind barrier can also prevent the movement of sand particles, reduce the deposition of sand particles on the embankment and track, and reduce the impact and erosion of sand particles on the HST surface. In order to analyze the effect of wind barriers on the movement and deposition of sand particles, the 3D volume fraction distributions of the sand phase are given in Figure 19, and the 2D volume fraction distribution of the middle cross section of the HT, MT and TT are also given in Figure 20. The turbulent kinetic energy (TKE) distributions of the HST' cross-section is given in Figure 21.

As shown in Figure 19: when the HST exits the tunnel, it suddenly encounters a wind-sand flow, and the thin layer sand is attached to the surface of the streamlined nose of HT. There is a large amount of sand particles deposited on the WS of the tunnel entrance, and there is a risk of the tunnel entrance being buried over time. Under the continuous impact of the wind-sand flow, the nose surface is eroded by the sand particles. Many sand particles remaining on the surface of the streamlined nose, which may seriously affect the driver's visibility. The entire carriage is covered with a large number of sand particles due to the bypassing effect of the air flow (especially at the joints of the carriages). Sand particles are deposited on the LS of the track due to the response of the embankment and track to wind-sand flow. As the train passes, the train winds swirl the sand particles around the embankment and track mixing with airborne sand particles and moving with the vortex structures shed on the TT, eventually settling around the track. There, there are fewer sand particles attached to the TT's surface, and the track over which the train travels accumulates a lot of deposited sand particles. The sand particles on the track slab will cause great harm to the bogies and wheels of the HST, so it is necessary to take measures to prevent the sand particles from being deposited on the track or to clean the accumulated sand on the HSRL in time.

When the HSRL is not protected by the wind barrier, pulsating wind-sand flows move to the embankment and track system and sand particles are deposited on the LS of the track slab. Under the impact of the wind-sand flow, the nose of the HT is severely eroded and many sand particles are attached to the nose of the HT. When there is the wind barrier on the embankment, the wind barrier changes the flow structure of the wind-sand flow and the trajectory of the sand particles. The train surface and track plate are almost free of sand particles attachment and deposition.

As shown in Figure 20: the wind drives the sand particles into motion, the sand particles mainly exist in the high wind speed region and the vortex. The wind-sand flow bypasses the HST's top to form a vortex on the LS of the HST. Sand particles are swept up by the airflow and impacted on the WS of the HST, and then deposited on the LS of the HST bypassing the roof of the HST. Sand particles are distributed in strips and vortices in the vicinity of the HST due to the accelerating effect of bypassing

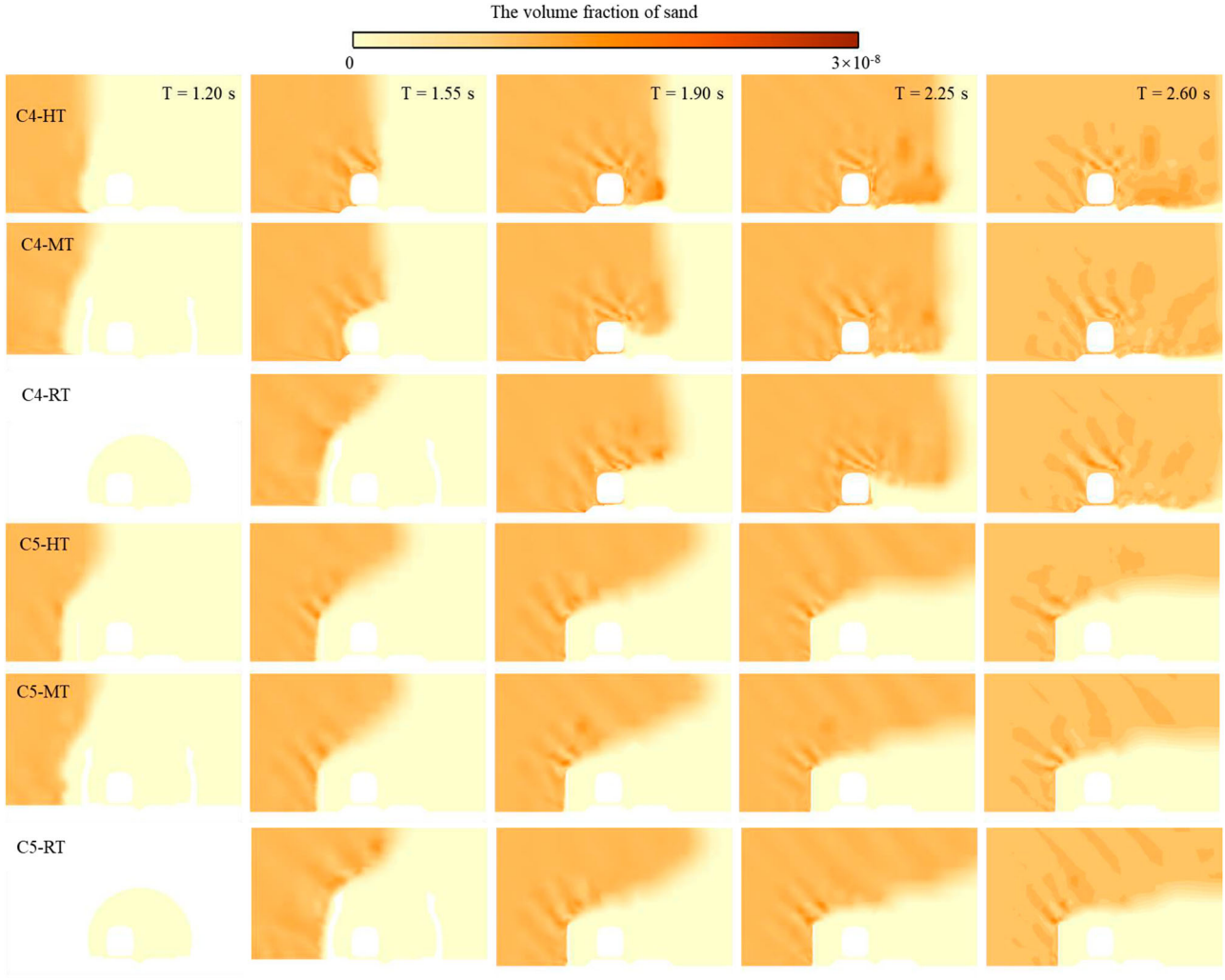

Figure 20. 2D volume fraction distribution of the middle cross section.

and sand particles concentrate on solid surfaces, and sand particles are distributed in strips as they follow the airflow around the WS and top of the HST. The airflow bypasses the carriage and forms a vortex on the LS, and the sand particles are involved in the vortex and move along with it, so the sand particles are distributed in a vortex shape on the LS of the carriage. When the wind barrier is installed on the HSRL, the top of the wind barrier has an accelerating effect on the wind-sand flow, and the airflow bypasses the embankment and track. Most of the lightweight sand particles bypass the wind barrier's top with the airflow, avoiding deposition on the HSRL and significantly reducing the harm to the HSTs and track structures.

As shown in Figure 21: when the HST is running on the HESL, there is a large area of strong TKE region on the LS of the HT and the ground of the embankment under the impact of the wind-sand flow, so the sand particles deposited on the embankment are swept up by the airflow; for the MT, the strong TKE region shifts to the roof and bottom of the LS, and the sand particles rise with the vortex. For the TT, the intensity of TKE decreases, and the sand particles are dispersed with the tail vortex and deposited again on the track.

5. Conclusions

Based on the multiphase flow and SST *k-w* model, the variation law of the HST's ALs at tunnel-embankment scenarios under different wind-sand flow conditions is investigated. The motion and deposition characteristics of pulsating wind-sand flow on the tunnel-embankment under the disturbance of wind barrier are revealed. The results of the study prove that the pulsating wind-sand flow has the greatest impact on the operational safety of HST, and the single-side solid wind barrier can considerably reduce the HST's aerodynamic load fluctuation. The wind-sand flow modelling method proposed in the paper

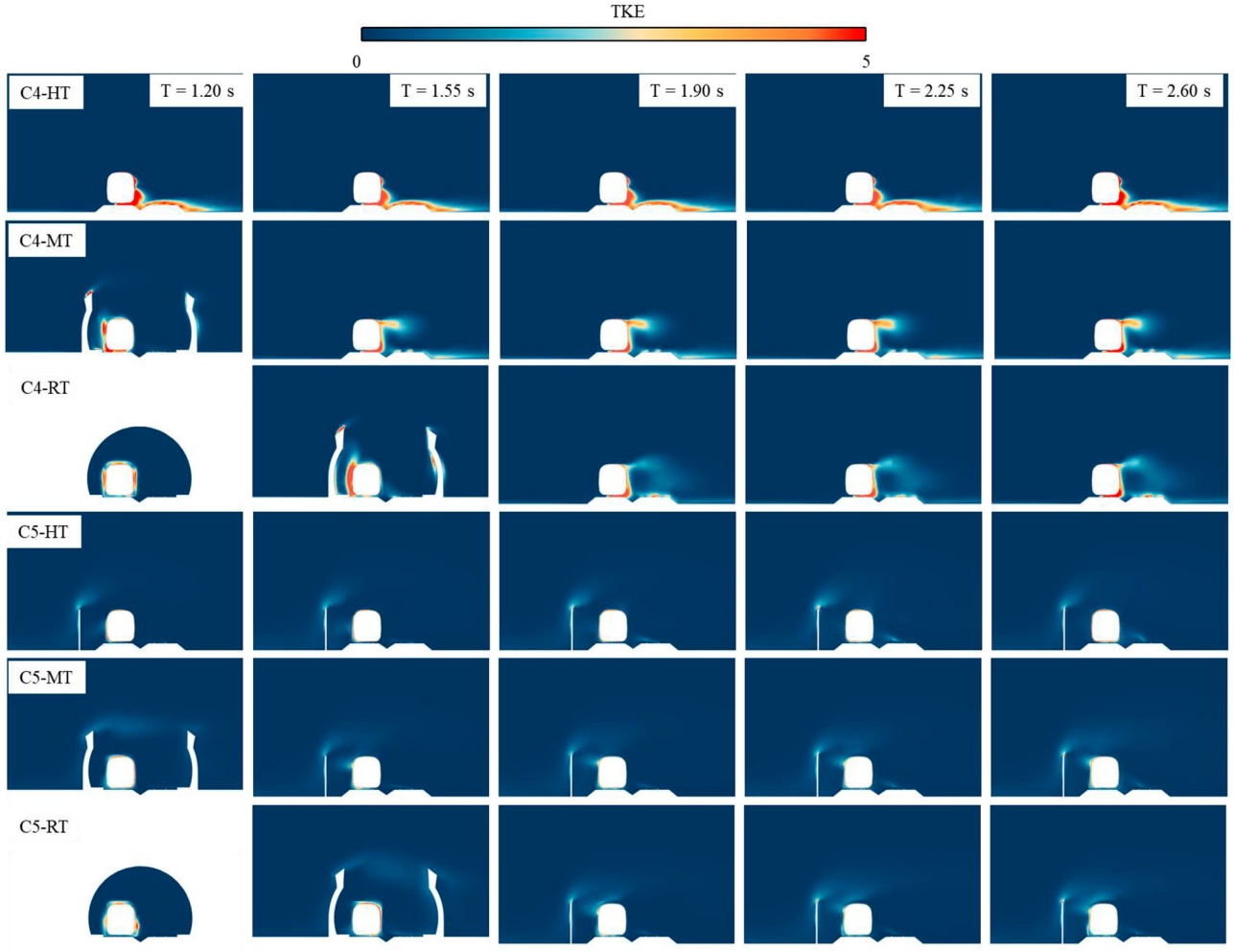

Figure 21. The turbulent kinetic energy (TKE) distributions of the HST.

provides a new research scheme for wind-sand flow control and HSTs' operational safety protection. The main conclusions are as follows:

(1) Under pulsating wind-sand flow, the five AL coefficients have the greatest amplitude of maximum value, and the HST's operation safety is most affected. When sand particles are wrapped in the air, the HST's ALs changes within 9.09%.
(2) Compared with the constant wind, the pulsating wind causes the fluctuation of the HST's ALs, and the maximum AL coefficient has a difference of 96.11%, which will cause the HST' carriages vibration.
(3) Under the impact of wind-sand flow, a large number of sand particles are deposited on the WS of the tunnel entrance and the embankment, there is a risk that the tunnel entrance and track could be buried without protection of the wind barrier. The streamlined nose of the HST is impacted by the wind-sand flow, and many sand particles deposit on the surface of the streamlined nose.
(4) The single-side solid wind barrier has a significant disturbing effect on wind-sand flow. The wind barrier changes the flow field mechanism around the HST, and the HST's ALs fluctuation are dramatically reduced. The maximum values of C_y, C_z, C_{mx}, C_{my} and C_{mz} of the HT are reduced by 85.75, 64.46, 50.00, 81.35 and 46.53%, respectively.
(5) The wind barrier disturbs the movement and deposition pattern of the wind-sand flow. Lightweight sand particles bypass the top of the wind barrier with the airflow and are not deposited on the embankment and track for a short period, and the erosion of the HST's surface is sharply reduced.

The limitation of this study is the lack of wind tunnel experiments for aerodynamic performance of moving trains at the tunnel entrance under wind and sand flow. In addition, the Euler two-phase flow method used in the study is unlikely to simulate the motion patterns of individual sand grains well. Therefore, a comparative study of the motion of sand particles

can be carried out by combining the Euler–Lagrange method.

The paper discusses and analyzes the transient aerodynamic performance of a train under wind-sand flow. The dynamic response and the safety performance of the train under wind-sand flow are the focus of the next research. The wheel-rail contact relationship between the wheels and the rails of HSTs will change under the action of sand particles. The friction between the rails and the wheels may be reduced and the trains' derailment possibility will be much higher. In addition, sand particles may cause the wave abrasion effect on the rails, thus affecting the service life of the rails and the operational safety of HSTs.

Disclosure statement

No potential conflict of interest was reported by the author(s).

Funding

This work was funded by the National Natural Science Foundation of China [52308419], the Research Grants Council (RGC) of the Hong Kong Special Administrative Region (SAR) Government [R-5020-18], the Innovation and Technology Commission of the Hong Kong SAR Government [K-BBY1] and The Hong Kong Polytechnic University's Postdoc Matching Fund Scheme [1-W21Q].

References

Arias-Cuevas, O., Li, Z. L., & Lewis, R. (2011). A laboratory investigation on the influence of the particle size and slip during sanding on the adhesion and wear in the wheel–rail contact. *Wear*, *271*(1-2), 14–24. https://doi.org/10.1016/j.wear.2010.10.050

Bruno, L., Fransos, D., & Giudice, A. L. (2018a). Solid barriers for windblown sand mitigation: Aerodynamic behavior and conceptual design guidelines. *Journal of Wind Engineering and Industrial Aerodynamics*, *173*, 79–90. https://doi.org/10.1016/j.jweia.2017.12.005

Bruno, L., Horvat, M., & Raffaele, L. (2018b). Windblown sand along railway infrastructures: A review of challenges and mitigation measures. *Journal of Wind Engineering and Industrial Aerodynamics*, *177*, 340–365. https://doi.org/10.1016/j.jweia.2018.04.021

Carrascal, I. A., Casado, J. A., Diego, S., & Polanco, J. A. (2016). Dynamic behaviour of high-speed rail fastenings in the presence of desert sand. *Construction and Building Materials*, *117*, 220–228. https://doi.org/10.1016/j.conbuildmat.2016.05.023

Deng, E., Yang, W. C., Lei, M. F., Zhu, Z. H., & Zhang, P. P. (2019). Aerodynamic loads and traffic safety of high-speed trains when passing through two windproof facilities under crosswind: A comparative study. *Engineering Structures*, *188*(1), 320–339. https://doi.org/10.1016/j.engstruct.2019.01.080

Deng, E., Yue, H., Ni, Y. Q., He, X. H., Yang, W. C., & Chen, Z. W. (2023). Wake dynamic characteristics of windproof structures in embankment–bridge sections along a high-speed railway under natural strong crosswinds. *Physics of Fluids*, *35*(5), 055109. https://doi.org/10.1063/5.0147079

Deng, G. X., Ma, W., Peng, Y., Wang, S. M., Yao, S., & Peng, S. (2021). Experimental study on laminated glass responses of high-speed trains subject to windblown sand particles loading. *Construction and Building Materials*, *300*, 124332. https://doi.org/10.1016/j.conbuildmat.2021.124332

Faccoli, M., Petrogalli, C., Lancini, M., Ghidini, A., & Mazzù, A. (2018). Effect of desert sand on wear and rolling contact fatigue behaviour of various railway wheel steels. *Wear*, *396-397*, 146–161. https://doi.org/10.1016/j.wear.2017.05.012

Giudice, A. L., & Preziosi, L. (2020). A fully Eulerian multiphase model of windblown sand coupled with morphodynamic evolution: Erosion, transport, deposition, and avalanching. *Applied Mathematical Modelling*, *79*, 68–84. https://doi.org/10.1016/j.apm.2019.07.060

Hao, Y. H., Feng, Y. J., & Fan, J. C. (2016). Experimental study into erosion damage mechanism of concrete materials in a wind-blown sand environment. *Construction and Building Materials*, *111*, 662–670. https://doi.org/10.1016/j.conbuildmat.2016.02.137

He, C. G., Zou, G., Gan, Y. Z., Ye, R. W., Zhai, Y. J., & Liu, J. H. (2023). Analysing the rolling contact damage behavior of a high-speed wheel tread - A case study. *Wear*, *522*, 204677. https://doi.org/10.1016/j.wear.2023.204677

He, P. L., Zhang, J., Herrmann, H. J., & Huang, N. (2022). Large-eddy simulation of wind-blown sand under unstable atmospheric boundary layer. *Science Bulletin*, *67*(14), 1421–1424. https://doi.org/10.1016/j.scib.2022.05.011

He, X. H., Fang, D. X., Li, H., & Shi, K. (2019). Parameter optimization for improved aerodynamic performance of louver-type wind barrier for train-bridge system. *Journal of Central South University*, *26*(1), 229–240. https://doi.org/10.1007/s11771-019-3996-8

He, X. H., & Li, H. (2020). Review of aerodynamics of high-speed train-bridge system in crosswinds. *Journal of Central South University*, *27*(4), 1054–1073. https://doi.org/10.1007/s11771-020-4351-9

Horvat, M., Bruno, L., & Khris, S. (2021). CWE study of wind flow around railways: Effects of embankment and track system on sand sedimentation. *Journal of Wind Engineering and Industrial Aerodynamics*, *208*, 104476. https://doi.org/10.1016/j.jweia.2020.104476

Horvat, M., Bruno, L., & Khris, S. (2022). Receiver sand mitigation measures along railways: CWE-based conceptual design and preliminary performance assessment. *Journal of Wind Engineering and Industrial Aerodynamics*, *228*, 105109. https://doi.org/10.1016/j.jweia.2022.105109

Huang, B., Li, Z. N., Gong, B., Zhang, Z. T., Shan, B., & Pu, O. (2023). Study on the sandstorm load of low-rise buildings via wind tunnel testing. *Journal of Building Engineering*, *65*, 105821. https://doi.org/10.1016/j.jobe.2022.105821

Huang, B., Li, Z. N., Zhao, Z. F., Wu, H. H., Zhou, H. F., & Cong, S. (2018). Near-ground impurity-free wind and wind-driven sand of photovoltaic power stations in a desert area. *Journal of Wind Engineering and Industrial Aerodynamics*, *179*, 483–502. https://doi.org/10.1016/j.jweia.2018.06.017

Jiang, Y. S., Gao, Y. H., Dong, Z. B., Liu, B. L., & Zhao, L. (2018). Simulations of wind erosion along the qinghai-Tibet railway in north-central Tibet. *Aeolian Research*, *32*, 192–201. https://doi.org/10.1016/j.aeolia.2018.03.006

Kian, A. R. T., Sadeghi, J., & Zakeri, J. A. (2022). Influences of railway ballast sand contamination on loading

pattern of pre-stressed concrete sleeper. *Construction and Building Materials*, *233*, 117324. https://doi.org/10.1016/j.conbuildmat.2019.117324

Li, T., Dai, Z., Yu, M., & Zhang, W. (2021a). Numerical investigation on the aerodynamic resistances of double-unit trains with different gap lengths. *Engineering Applications of Computational Fluid Mechanics*, *15*(1), 549–560. https://doi.org/10.1080/19942060.2021.1895321

Li, T., Qin, D., & Zhang, J. Y. (2019). Effect of RANS turbulence model on aerodynamic behavior of trains in crosswind. *Chinese Journal of Mechanical Engineering*, *32*(5), 12.

Li, Z. N., Pu, O., Gong, B., Zhao, Z. F., Bing, B., & Wu, H. H. (2021b). A new method of measuring sand impact force using piezoelectric ceramics. *Measurement*, *179*, 109390. https://doi.org/10.1016/j.measurement.2021.109390

Masoud, M., & Amir, M. S. (2021). The optimum model determination of porous barriers in high-speed tracks. *Journal of Rail and Rapid Transit*, *236*(1), 15–25.

Masoud, M., & Mohammad, A. R. (2013). Numerical calculations of aerodynamic performance a regional passenger train at crosswind conditions. *International Journal of Vehicle Structures and Systems*, *5*(2), 68–74.

Masoud, M., & Mohammad, A. R. (2018a). Two-dimensional analysis of the influence of windbreaks on airflow over a high-speed train under crosswind by using lattice boltzmann method. *Proceedings of the Institution of Mechanical Engineers, Part F: Journal of Rail and Rapid Transit*, *232*(3), 863–872. https://doi.org/10.1177/0954409717699502

Masoud, M., & Mohammad, A. R. (2018b). Multi objective optimization of aerodynamic design of high speed railway windbreaks using lattice Boltzmann method and wind tunnel test results. *International Journal of Rail Transportation*, *6*(3), 183–201. https://doi.org/10.1080/23248378.2018.1463873

Masoud, M., Yuan, M., & Rasul, M. (2023). The analysis of utilizing multiple fences in high-speed tracks on the aerodynamic characteristics of a high-speed train model. *Iranian Journal of Science and Technology, Transactions of Mechanical Engineering*,

Mehdipour, R., & Baniamerian, Z. (2019). A new approach in reducing sand deposition on railway tracks to improve transportation. *Aeolian Research*, *41*, 100537. https://doi.org/10.1016/j.aeolia.2019.07.003

Niu, J. Q., Zhang, Y. C., Li, R., Chen, Z. W., Yao, H. D., & Wang, Y. M. (2022). Aerodynamic simulation of effects of one- and two-side windbreak walls on a moving train running on a double track railway line subjected to strong crosswind. *Journal of Wind Engineering and Industrial Aerodynamics*, *221*, 104912. https://doi.org/10.1016/j.jweia.2022.104912

Paz, C., Suárez, E., Gil, C., & Concheiro, M. (2015). Numerical study of the impact of windblown sand particles on a high-speed train. *Journal of Wind Engineering and Industrial Aerodynamics*, *145*, 87–93. https://doi.org/10.1016/j.jweia.2015.06.008

Raffaele, L., Beeck, J. V., & Bruno, L. (2021). Wind-sand tunnel testing of surface-mounted obstacles: Similarity requirements and a case study on a sand mitigation measure. *Journal of Wind Engineering and Industrial Aerodynamics*, *214*, 104653. https://doi.org/10.1016/j.jweia.2021.104653

Sarafrazi, V., & Talaee, M. R. (2020). Simulation of wall barrier properties along a railway track during a sandstorm. *Aeolian Research*, *46*, 100626. https://doi.org/10.1016/j.aeolia.2020.100626

Tan, L. H., Qu, J. J., Wang, T., Zhang, W. M., Zhao, S. P., & Wang, H. T. (2022). Vertical flux density and frequency profiles of wind-blown sand as a function of the grain size over gobi and implications for aeolian transport processes. *Aeolian Research*, *55*, 100787. https://doi.org/10.1016/j.aeolia.2022.100787

Tan, L. H., Zhang, W. M., Qu, J. J., Wang, J. Z., An, Z. S., & Li, F. (2016). Aeolian sediment transport over gobi: Field studies atop the mogao grottoes, China. *Aeolian Research*, *21*, 53–60. https://doi.org/10.1016/j.aeolia.2016.03.002

Tominaga, Y., Okaze, T., & Mochida, A. (2018). Wind tunnel experiment and CFD analysis of sand erosion/deposition due to wind around an obstacle. *Journal of Wind Engineering and Industrial Aerodynamics*, *182*, 262–271. https://doi.org/10.1016/j.jweia.2018.09.008

Wang, S. M., Peng, Y., Chen, X. Z., & Wang, K. (2022a). The crack propagation and dynamic impact responses of tempered laminated glass used in high-speed trains. *Engineering Failure Analysis*, *134*, 106024. https://doi.org/10.1016/j.engfailanal.2021.106024

Wang, T., Qu, J. J., & Tan, L. H. (2023). Aeolian sediment transport over sandy gobi: Field studies in the nanhu gobi along the hami-Lop Nor railway. *International Soil and Water Conservation Research*, *11*(1), 125–134. https://doi.org/10.1016/j.iswcr.2022.03.009

Wang, T., Qu, J. J., Tan, L. H., Gao, Y., Zhang, K., & Shi, B. Y. (2022b). Aeolian sediment transport over the gobi with high gravel coverage under extremely strong winds in the hundred miles windy area along the lanzhou-xinjiang high-speed railway. *Journal of Wind Engineering and Industrial Aerodynamics*, *220*, 104857. https://doi.org/10.1016/j.jweia.2021.104857

Xiong, H. B., Yu, W. G., Chen, D. W., & Shao, X. M. (2011). Numerical study on the aerodynamic performance and safe running of high-speed trains in sandstorms. *Journal of Zhejiang University-SCIENCE A*, *12*(12), 971–978. https://doi.org/10.1631/jzus.A11GT005

Yang, W. C., Yue, H., Deng, E., He, X. H., Zou, Y. F., & Wang, Y. W. (2020). Comparison of aerodynamic performance of high-speed train driving on tunnel-bridge section under fluctuating winds based on three turbulence models. *Journal of Wind Engineering and Industrial Aerodynamics*, *228*, 105081. https://doi.org/10.1016/j.jweia.2022.105081

Yao, Z. Y., Xiao, J. H., & Jiang, F. Q. (2012). Characteristics of daily extreme-wind gusts along the lanxin railway in xinjiang, China. *Aeolian Research*, *6*, 31–40. https://doi.org/10.1016/j.aeolia.2012.07.002

Zhang, J. Y., Zhang, M. J., & Li, Y. L. (2019). Aerodynamic effects of subgrade-tunnel transition on high-speed railway by wind tunnel tests. *Wind and Structures*, *28*(4), 203–213.

Zhang, M. Y., Xiao, H., Mahantesh, M. N., Jin, F., & Liu, G. P. (2020). Track structure failure caused by sand deposition: Simulation and experimentation. *Aeolian Research*, *43*, 100578. https://doi.org/10.1016/j.aeolia.2020.100578

Zhang, Z. H., Xiao, H., Wang, M., Zhang, M. Y., & Wang, J. Q. (2021). Research on dynamic mechanical behavior of ballast bed in windblown sand railway based on dimensional analysis. *Construction and Building Materials*, *278*, 123052. https://doi.org/10.1016/j.conbuildmat.2021.123052